J Mater Sci (2011) 46:3356–3369
DOI 10.1007/s10853-010-5224-7

AFM analysis of the surface of nanoporous membranes: application to the nanofiltration of potassium clavulanate

A. L. Carvalho · F. Maugeri · V. Silva · A. Hernández · L. Palacio · P. Pradanos

Received: 22 October 2010 / Accepted: 24 December 2010 / Published online: 14 January 2011
© Springer Science+Business Media, LLC 2011

Abstract This study presents the structural characterization of the surface of four commercial nanofiltration membranes: NF90 (polyamide) and NF (polypiperazine amide) from Filmtec™ and NP010 and NP030 (polysulfone) from Microdyn Nadir®, by Atomic Force Microscopy (AFM). These membranes have been studied before and after undergoing a filtration process with potassium clavulanate. The fast Fourier filtering of AFM images with very high magnification (40 × 40 nm) has allowed identifying the pore size distribution and geometry of the pores on the surface of the membrane before their use. Images between 0.5 × 0.5 and 10 × 10 μm^2 have allowed the study of the surface roughness of the samples before and after being used to filtrate potassium clavulanate solutions. The results of roughness and power spectral fractal dimension along with the skewness and kurtosis of the height distribution have been analyzed in terms of pore size, hydraulic permeability, and the adsorption of clavulanate for the different samples.

Introduction

Nanofiltration is a relatively new pressure driven membrane process that has properties in between ultrafiltration and reverse osmosis. The main advantages of this process are: operation at low pressures when compared to reverse osmosis, high fluxes, considerable retention of multivalent anionic salts, and low molecular weight organic molecules, relatively low investment, and low cost of operation and maintenance with a low energy consumption [1]. It has applications in a wide range of fields that include fractionation and selective removal of solutes from complex process streams with rejection of ions and charged organic pollutants [2, 3]. In the food industry, it has been used for the demineralization of whey and the fractionation [4], etc. It is considered the most important recent development in process engineering and environmental protection [2, 5, 6].

The characterization of nanofiltration membranes includes the use of predictive models, which help to understand the separation process. Because the morphological properties of the membranes have important consequences on performance and fouling, it is very important to characterize them by experimental techniques that could determine their structure and pore distribution [2, 6–11].

Despite the efforts that could be made to minimize the fouling caused by the membrane-solute affinity, it occurs in many instances [12] and it is perhaps the most critical parameter in membrane filtration [12–15]. This is the reason why nanofiltration membranes, although having many applications [16–19], are not still reached their potential on an industrial scale. Fouling increases the operation and maintenance costs, it causes a decline in the permeate flux, and increments in the energy demands, turning down the membrane performance and ultimately reducing membranes life [13, 20, 21].

An understanding of the relationship between membrane surface properties and separation characteristics can determine the choice of a membrane for a particular separation and can lead to the development of membrane

A. L. Carvalho · F. Maugeri
Department of Food Engineering, Faculty of Food Engineering, University of Campinas—UNICAMP, Rua Monteiro Lobato 80, Barão Geraldo, CEP: 13083-862 Campinas, SP, Brazil

V. Silva · A. Hernández (✉) · L. Palacio · P. Pradanos
Departamento de Fisica Aplicada, Facultad de Ciencias, Universidad de Valladolid, Real de Burgos s/n, 47071 Valladolid, Spain
e-mail: tonhg@termo.uva.es

technology too [7]. Some of the most important surface characteristics are the mean pore size and the pore size distribution, the pore density, and the surface roughness. The pore size plays an important role in the transport through the membrane, because it determines rejection and selectivity along with flux or permeability [7, 12, 22, 23].

There are several well-established techniques for the determination of the pore size distributions and porosity. They include the bubble point technique, mercury porosimetry, the microscopic technique, solute transport, permporometry, and thermoporometry [7]. Many advances in the study of membrane structure have been made possible [24] by microscopic techniques such as: Scanning Electron Microscopy, SEM, [25], Transmission Electron Microcopy, TEM, [26], Atomic Force Microscopy, AFM, [6], and Scanning Tunneling Microscopy, STM, [27]. This is especially true for nanofiltration membranes that are nanoporous in nature; i.e., they have pores in the nanometric range.

Among the microscopic techniques, AFM is a relatively recent technique. It gives topographical images of the membrane surface by scanning with a sharp tip over the surface without any previous sample preparation. Since its invention, AFM has been applied to study microfiltration, ultrafiltration membranes [9, 27–31], and more recently nanofiltration membranes [3, 6, 7, 10, 32–36] and other nanoporous materials [37–40]. This technique allows characterizing membranes surfaces, including non-conducting surfaces with a nanometer (or even atomic) resolution in wet and dry environments. AFM allows also the study of the adhesion of particles and the properties of the subsequent deposit during fouling.

Most investigations have focused on the pore structure disregarding other important parameters that might be taken into account. Nevertheless, it is obvious that the pore size distribution alone does not describe completely the morphology of the membrane. In this sense, surface topography plays an important role in determining the fouling properties. Rough materials have more surface area, and the fluid mechanics on them can also influence the resulting fouling rates. Very often, roughness is determined by using, for example, the average or the root-mean-square. Other complementary parameters are also interesting as skewness and kurtosis which describe the peak asymmetry and flatness, respectively, of the heights distribution on the surface. Moreover, most researchers appear to be unaware that several of these roughness measurements are scale dependent and dismiss the fractal dimension that is a key scale independent parameter reflecting the roughness [11, 28].

Clavulanic acid, CA, is a compound produced by *Streptomyces clavuligerus*, and it consists of a β-lactam ring fused to an oxozilidine ring [41]. It shows weak antibacterial activity against most bacteria, but is a potent inhibitor of a wide range of β-lactamase and is able to potentiate the antibacterial activity of penicillins and cephalosporins against many β-lactamase-producing resistant bacteria [42]. It is currently used in combination with amoxicillin or other semi-synthetic penicillins for the treatment of infections caused by β-lactamase-producing bacteria. CA is produced industrially by fermentation and is isolated and purified from the fermentation medium in several steps. The first step involves clarification of the medium by filtration or centrifugation followed by either adsorption or liquid–liquid extraction with an organic solvent, normally butanol. Further purification is achieved by anion-exchange chromatography.

It is known that the CA is chemically unstable to temperatures over 30 °C and pH over 7.5 or below 4.5 [43, 44]. Owing to this unstable nature of the free acid, CA is isolated as the lithium, potassium, or sodium salt. A picture of the molecular structure of both the CA and the potassium clavulanate, KCA, are shown in Fig. 1.

Attending to its molecular weight, see Fig. 1, nanofiltration seems fully adequate for the purification of KCA. This raises some problems due to the high fouling levels appearing. In order to design an adequate process, nanofiltration with membranes with pores in the nanometer range with low fouling should be sought. Furthermore, the characterization of some potentially appropriate membranes can be profited to test how AFM techniques can help in this process.

By using AFM, the pore size of four commercially available membranes, with appropriate characteristics, will be studied. AFM is also uniquely qualified to investigate the dominant factors associated in the adsorption of solutes on surfaces with variation of surface topography at nanoscale resolution [45, 46]. Thus, the morphology of these membranes will be studied, before and after their use to concentrate KCA, by analyzing their surface roughness and fractal dimension. This will be done to analyse how KCA is deposited on the membranes and trying to correlate these parameters with the reduction in flux.

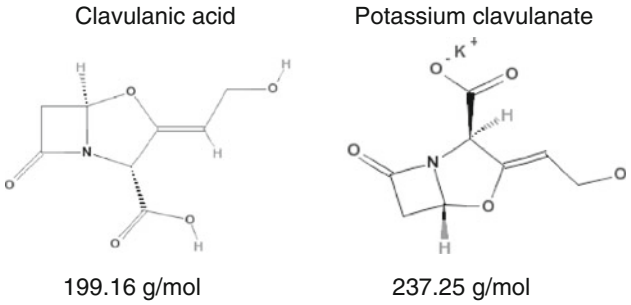

Fig. 1 Molecular structure of both the clavulanic acid and the potassium clavulanate

Methodology

Membranes and chemicals

Four commercial membranes have been selected and studied here. Two of them are made from polyamides: NF (polypiperazine amide) and NF90 (fully aromatic polyamide [15, 47]) membranes from Filmtec™. Another two membranes, NP010 and NP030, are made from polyethersulfone and manufactured by Microdyn Nadir®. Table 1 shows the main characteristics of these membranes according to their manufacturers.

Milli-Q quality water has been used both for water permeability measurements and for the aqueous solution filtration experiments. These solutions were prepared with KCA salt. They were vacuum filtered and micro-filtered in 14 and 0.45 μm pore membranes, respectively. The pH of the KCA solutions was adjusted to 6.2 with HCl 0.2 N and KOH 1 M solutions prepared from analytical grade reagents from Probus and Panreac, respectively.

Nanofiltration experiments

Nanofiltration of KCA has been performed in a stainless steel stirred dead-end process that simulates a crossflow process. The system consists in a cylindrical container with a membrane located at its bottom and provided with a magnetic stirrer that simulates the convection in a crossflow process. Pressure differences have been applied by application of pressurized nitrogen, as shown in Fig. 2. The operational conditions consisted in: a stirring frequency of 600 rpm, an applied transmembrane pressure of 2×10^6 Pa, a volume of the feed phase of 200 mL, a process temperature of 25 °C, a pH of 6.2 and a KCA concentration on the feed phase of 750 mg/L. The process was stopped when the volume permeated arrived to 100 mL.

Table 1 Characteristics of the membranes used here as given by their manufacturers

Membrane	NF90	NF	NP030	NP010
MWCO (Da)	180[a]	>200	400	1000
Max. pressure (bar)	41	41	40	40
Max. temperature (°C)	45	45	95	95
pH range	2–11	3–10	0–14	0–14
Rejection (%)	>97[b]	>99[c]	80–95[d]	25–55[d]

[a] Molecular weight cut off according to Lopez Muñoz et al. [48] in Da (g/mol)

[b] Rejection of $MgSO_4$ (25 °C, 4.8 bar)

[c] Rejection of $MgSO_4$ (25 °C, 8.9 bar)

[d] Rejection of Na_2SO_4 (20 °C, 40 bar)

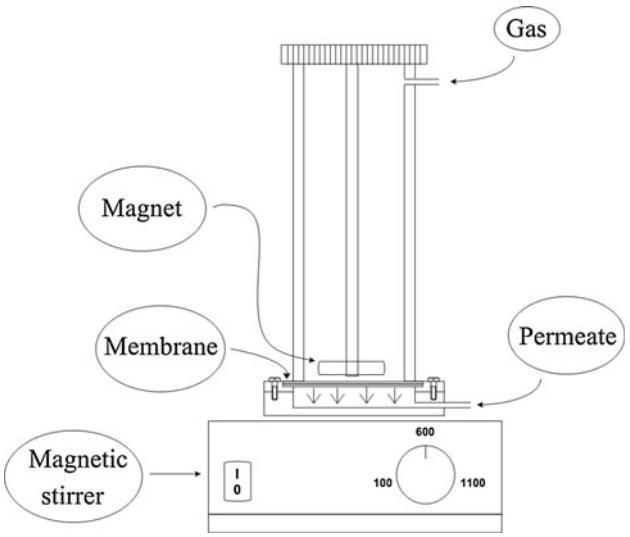

Fig. 2 Schematic representation of a crossflow nanofiltration experimental setup at laboratory scale

The water permeability has been determined from the variation of the flux with increasing pressure differences up to 4×10^6 Pa across the membrane at 25 °C. Water was passed under a 2×10^6 Pa pressure gradient through each membrane before and after its use with clavulanate, KCA until the resulting pure water flux remained constant.

Atomic force microscopy

With AFM images, we can study the topography of the surface of clean membranes as well as of the fouled ones. AFM has been performed with a Nanoscope Multimode IIIa scanning probe microscope from Digital Instruments (Veeco Metrology Inc., Santa Barbara, CA). Two scanners have been used: the J scanner with a maximum lateral (x, y) scan range of 115 μm and a maximum vertical (z) range of 5.5 μm for the biggest images; and the E scanner for the smallest areas analyzed (horizontal and vertical ranges of 10 and 2.5 μm, respectively). The scanned areas have gone from 40×40 nm to 100×100 μm. The smallest areas of 40×40 nm have only been used to get the accurate optimal resolution to detect the pore entrances. For scanned areas over 10×10 μm scratches and other surface damages are shown. Roughness has been measured for images from 0.5×0.5 to 10×10 μm.

For the images used to measure roughness, the resolution in the x–y scale decreases for increasing scanned areas because the size of the detectable details is $L/512$, L being the length of each side of the scanned square, this means that it goes from 1 to 20 nm. Referring to the z resolution, the corresponding set range has been appropriately reduced depending on the surface roughness to increase the z resolution. As a result, this zeta resolution is approximately of 0.2 nm in the worst case.

The contact mode of operation has been used for the most detailed pictures (40 × 40 nm images of clean membranes) while tapping (or intermittent contact) mode analysis has been used for the rest of the images.

In the intermittent contact operation mode, the tip and the supporting cantilever are made to oscillate close to their resonance frequency. In this case, it is not the cantilever deflection which is measured (as in conventional AFM techniques: both contact and non-contact methods), but the root mean square of the oscillation amplitude of the cantilever once it has been excited into resonance with a piezoelectric driver. The phase shift appearing at the resonance can be detected to give the so-called phase contrast images where the dominions with different viscoelastic properties can be easily detected. In any case, the tapping mode is an especially useful technique because it limits the possibility to damage both tip and sample due to their contact because it is the only intermittent.

In both the techniques used here (tapping and contact mode), the measurements have been performed in open atmosphere conditions and in the repulsive mode. Moreover, the tip always enters the condensation (contamination, humidity etc.) layer because the required strength is set adequately to overcome the capillary forces appearing in such a layer.

The tapping mode gives better-quality pictures than the non-contact mode but it is also free from the very typical artifacts obtained with the conventional contact method. Nevertheless, for the smallest images, used to determine the pore size distribution, the contact mode of operation has been used with a very low feed-back to measure heights by the cantilever deflection rather than by the vertical motion of the scanner that supports the sample. This method allows an increase in the scanning speed (without damages in tip and/or surface) that reduces noise and improves real resolution to reach even the atomic range [49]. This procedure can only be used for relatively flat surfaces. For larger scanned areas, due to the high roughness the feed-back system should act to avoid surface-tip crashing and consequently the tapping mode should be preferable due to the friction forces that would decrease resolution in the contact mode drastically.

The tapping mode has been performed by using the Olympus™ probes OMCL-AC160TS-W with a spring constant of 40 N/m. Drive frequency was determined by automatic tuning around 350 kHz at a target amplitude of 2 V. Tip velocities were adjusted according to the roughness of the sample and the size of the image. The curvature radius of this tip is below 10 nm. For the contact mode operation, Nanosensor® silicon tips of the CONTR#19809 type have been used. Their force constant is 0.12 N/m with a curvature radius below 10 nm. In both cases, the state of the tip has been tested before and after each experiment, and no significant variations have been detected. The test has been done by measuring the corresponding recommended standard calibration samples.

Tapping mode pictures (topographical images and phase contrast ones) have been acquired for each sample and focusing in areas randomly distributed on them. All images have been acquired with 512 points per scan line and with 512 lines. Images of 40 × 40 nm have been analyzed by using the command *Spectrum 2D*, function which transforms images by applying a 2D fast Fourier transform (FFT), to pass or remove specific frequencies from the images. This modification is necessary to eliminate the electrical noise and some other parasite vibrations (that affect specially the high resolution images). The image acquisition and treatment have been done with Nanoscope Software, version 5.12 rev. B.

Surface analysis

A quantitative analysis of the roughness of the membrane has been performed, by using the Nanoscope Software functions. The surface roughness has been studied by statistical analysis of images with areas between 0.05 × 0.05 and 10 × 10 μm^2.

A common quantification of surface roughness is the root-mean-square roughness RMS or S_q:

$$S_q = \sqrt{\frac{\sum_{i=1}^{N_t} (z - \bar{z})^2}{N_t}} \tag{1}$$

referred to the average height,

$$\bar{z} = \frac{\sum_{i=1}^{N_t} z_i}{N_t} \tag{2}$$

where z_i is the deviation in height at the (x_i, y_i) point from the mean after baseline subtraction, and N_t is the total number of data points in the surface ($N_t = mN_l$ being m the number of lines and N_l the number of points per line) where z_i is collected. However, this parameter strongly depends on the instrument and the tip used and on the measurement procedure. In this sense [50], there is another parameter less dependent and based on a Fourier transform: the Power Spectra Density which analyses the two dimensional roughness spectra of the surface [51]. This spectrum can be evaluated as [24, 52]:

$$\gamma(p,q) = \gamma\left(p\Delta\sigma_x, q\Delta\sigma_y\right) = \left(\frac{2\pi}{L}\right)^2 |\hat{z}(p\Delta\sigma_x, q\Delta\sigma_x)|^2 \tag{3}$$

where

$$\Delta\sigma_x = \Delta\sigma_y = \frac{\pi}{N\Delta x} = \frac{\pi}{N\Delta y} = \frac{\pi}{L} \tag{4}$$

L being the length of each side of the scanned square, N is the number of points along each side of the square, Δx and

Δy are the distance between neighbor points along each direction on the scanned area. $\hat{z}$ is the discrete bi-dimensional Fourier transform of the height:

$$\hat{z}(p,q) = \frac{1}{4\pi^2}\left[\frac{L}{N}\right]^2 \times \sum_{m,n} z\left(m^L/_N, n^L/_N\right) \exp\left[-j\frac{2\pi}{N}[mp+nq]\right] \quad (5)$$

where $j = \sqrt{-1}$. Therefore

$$\gamma(\vec{\sigma}) = \gamma(p,q) = \frac{L^2}{4\pi^2 N^4}\left|\sum_{m,n} z\left(m^L/_N, n^L/_N\right) \exp\left[-j\frac{2\pi}{N}[mp+nq]\right]\right|^2 \quad (6)$$

The bi-dimensional spectrum $\gamma(\vec{\sigma})$, or even better its average on the polar angle $\gamma(\sigma)$ where $\sigma = |\vec{\sigma}|$ can be represented and allows to calculate the RMS roughness, S_q, as

$$S_q = \int_{\vec{\sigma}} \gamma(\vec{\sigma}) d\vec{\sigma} = 2\pi \int_{\sigma} \gamma(\sigma) d\sigma \quad (7)$$

The spatial pulsation σ has to be included in the interval:

$$\sigma \in \left[\frac{\pi}{L}, N\frac{\pi}{L}\right] \quad (8)$$

This methodology provides valuable information not only on the height deviation of the roughness profile, but also on its lateral distribution [53].

In a logarithmic scale, this spectrum has a linear behavior in very large ranges, according with the equation:

$$\gamma = \beta/\sigma^{\alpha} \quad (9)$$

β being a constant and α the spectrum slope. This power law is typical of fractal behavior of roughness (self-affine behavior). In this situation, the corresponding fractal dimension D can be evaluated as a function of the spectrum slope [24, 52]:

$$D = (8-\alpha)/2 \quad (10)$$

There are other useful parameters, two of them are especially significant and have been analyzed here:

- The surface skewness, S_{sk}, related to the third moment of the height of the distribution, which informs about the asymmetry relative to Gaussian distribution. For a set of discrete data can be calculated as [54]:

$$S_{sk} = \frac{1}{N_t S_q^3}\sum_{i=1}^{N_t} (z_i - \bar{z})^3 \quad (11)$$

- The surface kurtosis, S_{ku}, is a measure of how sharp the distribution is as compared to the Gaussian, and it is related to the fourth moment of the height of the distribution. It is calculated as:

$$S_{ku} = \frac{1}{N_t S_q^4}\sum_{i=1}^{N_t} (z_i - \bar{z})^4 \quad (12)$$

The pores size distributions have been obtained by computerized image analysis (CIA) from the same images. Image Analysis was carried out by means of Jandel® ScanPro software (version 3.00.0030), to study the pore size distribution. Each photograph was digitized with a resolution of 1024 × 768 pixels, assigning to each one a gray level ranging from 0 (black) to 255 (white). Then, clear-field equalization was applied to each image field to eliminate parasite changes in gray levels due to uneven bending. Once the bending effects were eliminated, the image gray spectrum was spanned to get the maximum contrast and definition. Then, the images were redefined according to an assigned gray threshold level under which every pixel was assigned to 1 and the rest to 0. The resulting binary picture was improved by scraping isolated pixels, in such a way that all the remaining 1's in the matrix were assumed to belong to a pore. Finally, the pore borders were smoothed to reduce the influence of the finite size of pixels and low definition. Of course a correct selection of threshold gray level is fundamental for correctly and accurately identifying pores. Customarily, the gray spectrum is analyzed and the threshold centred in the peak to peak valley of the almost bimodal distributions obtained. Unfortunately sometimes the spectra are so flat that this technique is only of relative help in making a correct threshold selection. In any case, inspection by eye facilitates the process of selection of several reasonable threshold candidates whose outcomes are averaged.

Results and discussions

Filtration processes

The water permeability (L_p) of each membrane has been determined before and after their use with KCA. All membranes were conditioned at the highest pressure allowed for each one, and the flows have been measured with time until becoming constant. This allows the hydration of the polymer material of the membrane and a correct measurement of the behavior of the equilibrated membrane [27]. The permeabilities of each membrane are presented in Table 2.

It is worth to note that the polyamide membranes (NF and NF90) have low initial permeabilities, but a quite small reduction in the flow after the filtering process, possibly due to a low affinity of the solute to the membrane surface. Polyethersulfone membranes (NP030 and NP010) have high initial permeabilities, nevertheless they suffer a more significant flux reduction, ending at low L_p, This behavior

Table 2 Water permeability for each membrane evaluated, before and after KCA permeation

L_p (10^{-11} m/Pa s)	NF90	NF	NP030	NP010
Before	1.53	3.39	4.36	6.47
After	1.10	2.46	1.96	1.38
L_p (used)/L_p (new) (%)	72	73	45	21

might be related to the chemical nature of the membrane materials, their electrical charge, and the morphological aspects of the membranes (pore size, porosity, and surface roughness) as well as to the operation conditions.

AFM characterization

Pore size distributions for clean membranes

For the clean membranes, it has been possible to obtain images which processed by FFT to eliminate noise, allow a visualization of the pores on the surface of the membrane. Figure 3a–d shows representative images for sampled areas of 40 × 40 nm^2. This results impossible for the KCA-fouled membranes because they appear as covered by an almost totally dense layer deposited KCA.

As Fig. 3 reveals, the four membranes analyzed present clear differences at the nanometer scale. The membrane NF90 has pores with mostly circular surface sections, whereas for the other three membranes (NF, NP010, and NP030) it is impossible to detect a regular geometry of the surface sections for their pores. Referring to the z-axis range, it is clear that it is larger for the NF90 (6 nm) and NF (4 nm) than for the polyethersulfone membranes ($\geq$1 nm).

The pore size distributions and the corresponding mean pore size for the membranes studied can be evaluated by CIA of the AFM images. Figure 4a–d shows the results obtained. It can be seen that the pore sizes follow Gaussian distributions. The mean pore size refers to the diameter on the entrance of the pores where AFM generally gives a funnel structure due to the tip-sample convolution [27] means that these pore sizes could be slightly overestimated [9]. All membranes present a mean pore size in the range of nanofiltration, with the sequence: NP010 > NP030 > NF > NF90, in the same order than their corresponding water permeability before being used with KCA and their nominal MWCO. The permeability–diameter relationship is not linear as shown in Fig. 5. This behavior is understandable, since the flow does not depend linearly on the pore size but on the squared diameter. The water permeability depends also on the density of pores per unit area according to the viscous flow regime.

To verify the validity of the distributions obtained, it is possible to compare the permeability obtained from the distribution (as predicted by the Hagen–Poiseuille law) with the experimental one. The Hagen–Poiseuille equation:

$$L_p = \sum_1^n \frac{\pi n_i r_i^4}{A\eta \Delta x} \tag{13}$$

where n_i is the number of pores per unit area of the membrane of the i-th class, r_i is the radius of these pores, η the water viscosity inside the pores, Δx thickness of the selective layer and A is 8 if the pores are assumed to have a cylindrical geometry or 3 if they are assumed to slit-like.

Moreover, to evaluate L_p, with Eq. 13, we need to do a series of considerations:

- It has been proved that the viscosity of aqueous solutions inside nanometric pores is enhanced due to confinement effects. It was calculated by Wesolowska et al. [55] and for these membranes the value used is 6.3 × 10^{-3} Pa s.
- The thickness of the active layer is a difficult parameter to be determined. It has to be taken into account that the thickness that should be required is the active layer one that is not always easy to detect because very frequently there is a gradual transition from the tight active layer to the porous support layer. For some nanofiltration membranes, this transition is sharp enough to be detected by using SEM images [56] giving values around 100 nm.

We compare the so obtained results for the water permeability with the experimental values in Fig. 6. The theoretical results for both the possible geometries (cylindrical or slit-like pores) are shown in this Figure. As mentioned, the NF90 membrane shows clear circular pore sections as shown in Fig. 3. So we could assume that all of them contain actually cylindrical pores. Thus, the differences between the experimental permeabilities and those predicted on the basis of the measured pore size distributions could be attributed to the membrane thickness that could be slightly different from that assumed in the calculations (100 mm). When this is taken into account, a fitted thickness could be evaluated to make coinciding experimental and theoretical values. This procedure gives the values shown in Table 3 for both the possible geometries. Note that these thicknesses are quite similar for the four membranes. This is why the lines in Fig. 6 resulted to be almost perfectly linear.

Comparing with the results on pure water permeability after KCA filtration, it can be noted that the membranes which seem to have the largest pores, before being used, do not present the highest flux. It can be due to the other factors that have also influence in the filtration process, as for example, the roughness or the hydrophobicity of the surface.

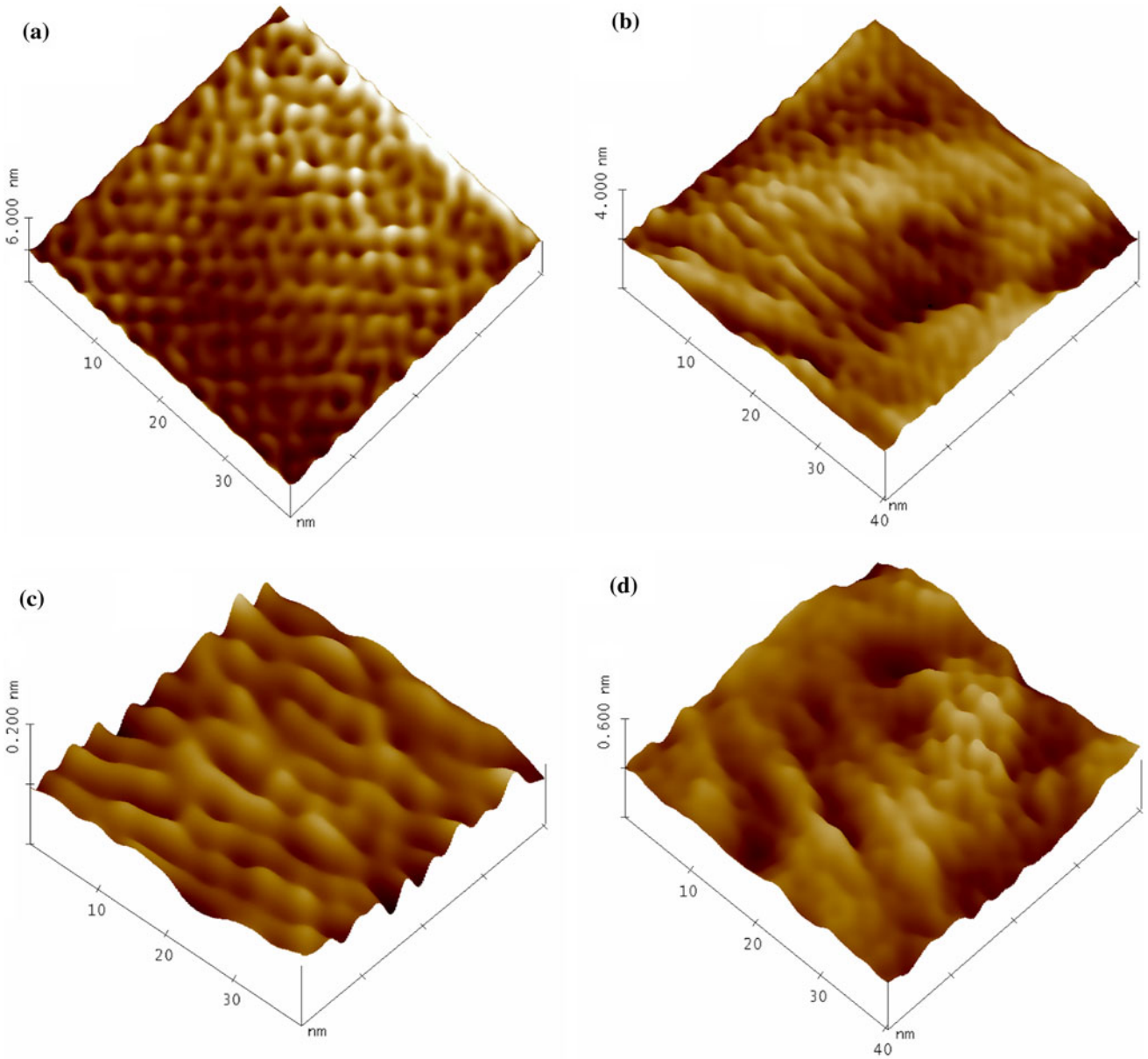

Fig. 3 Examples of the AFM images of the membranes with scanned areas of 40 × 40 nm^2 used to obtain the pore size distribution for: **a** NF90, **b** NF, **c** NP030, and **d** NP010

Comparing these results with those found in the literature, significant discrepancies are found. The NF membrane has only slightly larger sizes (between 3 and 13% depending on the conditions of measurement) than those found in the literature for neutral solute retention [4]. However, the NF90 presents pore sizes clearly larger than that found by Nghiem et al. [15] from solute retention and Hilal et al. [32] from AFM, which showed a mean value of 0.68 and 0.55 nm, respectively. A huge discrepancy was found for the NP010 membrane with a pore size of 0.33 nm from AFM [32].

One of the sources of these discrepancies can be that the samples were coming from different batches, what should be caused by a poor reproducibility of the membrane. In any case, it is known the existence of differences in the results obtained by different techniques [6]. As mentioned, the AFM technique is strongly influenced by the convolution between the tip curvature and the pore borders. Other problems, such as white thermal noise, causing spurious unwanted oscillation of the cantilever, should have been overcome because FFT filtering [5, 32] has been used.

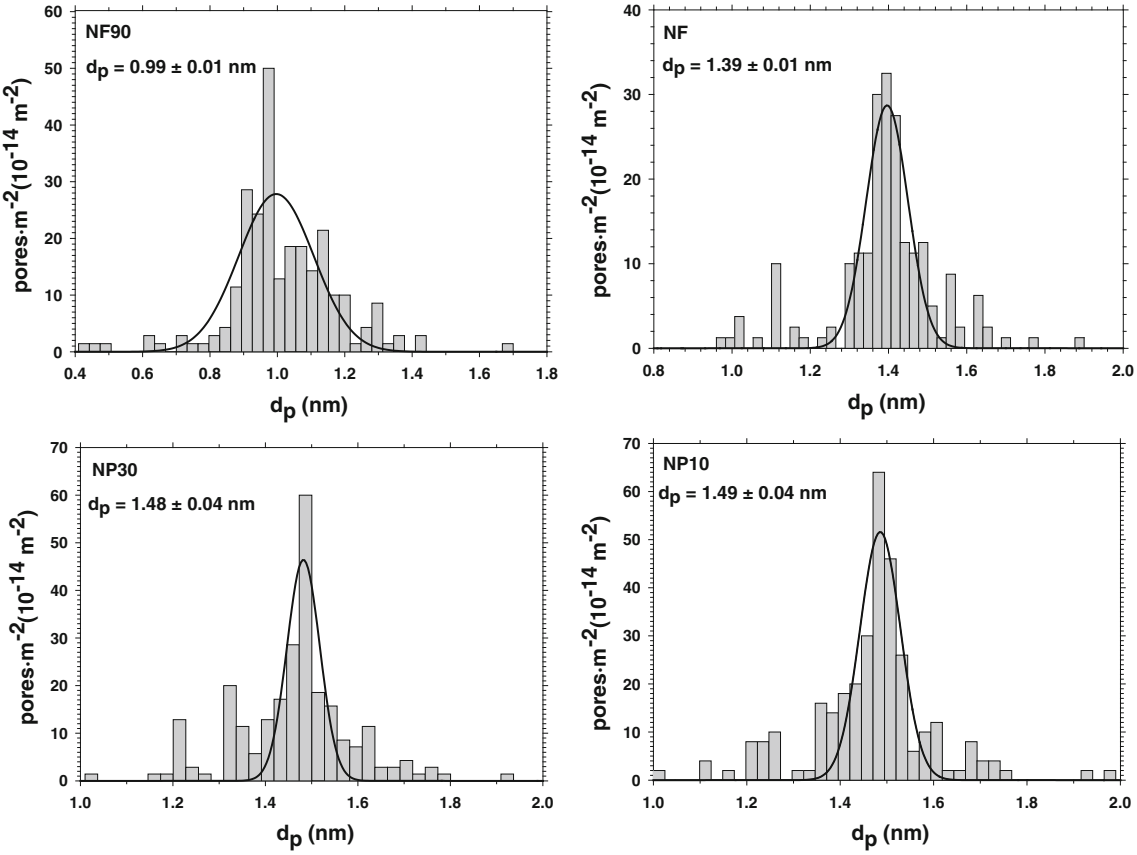

Fig. 4 Pore size distribution for the membranes NF90, NF, NP030, and NP010. They have been fitted to a Gaussian distribution showing the mean pore dimeter along with the standard deviation of the corresponding distribution

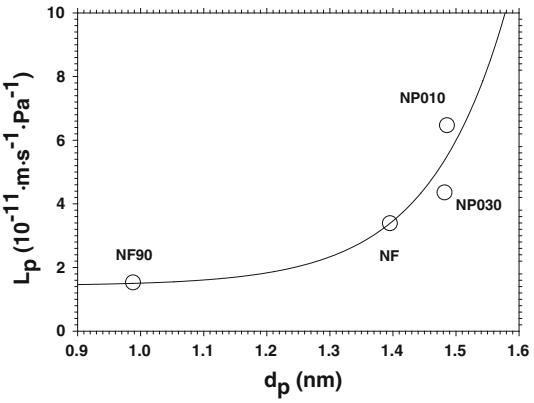

Fig. 5 Experimental water permeability versus mean pore diameters as obtained from AFM images

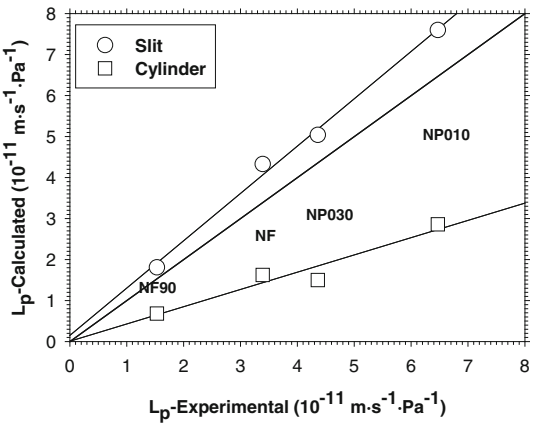

Fig. 6 Experimental permeability versus that calculated from the distributions shown in Fig. 4 and the Hagen–Poiseuille equation

This could justify the huge discrepancy between the value of pore diameter of the membrane NP010 found by us (1.5 nm) and by other authors (0.33 nm). However, the value of 0.33 nm for the pore size given in the literature for this membrane, NP010, which has a retention between 25 and 55% of Na_2SO_4 (see Table 1) does not seem very realistic. An ion of sulfate has a Stokes radius of 0.23 nm, which one would expect to be almost totally retained

Table 3 Membrane thickness in micrometer as obtained from the comparison of theoretical and experimental water permeabilities in Fig. 6

Membrane thickness (μm)	NF90	NF	NP030	NP010
Cylindrical pores	118.3	127.7	115.6	117.5
Slit-like pores	44.4	47.8	34.4	42.4

(retentions over a 90%) with a membrane with pore sizes of 0.33 nm.

Surface analysis

AFM has been used to study the morphology of the membranes and to evaluate the changes after the filtration of the synthetic solution of KAC described in the experimental section. In Fig. 7, images of the membranes obtained before and after filtration can be compared. In all cases, phase contrast images have been taken (but not shown here) to confirm that the membranes are totally covered by the foulant.

The NF90 membrane presents a similar structure before and after its use (Fig. 7a and b). In both cases, the surface is similarly highly rough. The lack of changes in this high roughness after filtration seems to indicate the appearance of a very thin layer of adsorption. In the case of NF membrane, (Fig. 7c and d), the surface is smoother than in the previous membrane, although it shows similar granular structures before and after the filtration of KCA. In this case, nothing can be concluded on the adsorption as far as it could be high but uniform, so it should lead to very slight changes in the morphology of the surface.

The NP030 membrane changed its structure from extremely smooth before the filtration to highly rough after its use, which indicates a high adsorption. This can be visualized in the Fig. 7e and f. Finally, the NP010 membrane presents a quite different structure after its use with a disappearance of the original topometry and the formation of a smooth morphology, as shown in the Fig. 7g and h.

From these results, it seems that the NF90 and possibly the NF membranes are less fouled by KCA. Probably, the KCA should interact less with the amide groups than with the sulfonic groups.

From the AFM images, the surface roughness was analyzed too. Figure 8a and b shows the variation of S_q with the length scale L for the membranes before and after KCA use, respectively. For non-used membranes, S_q increases with L until reaching a pseudo-plateau as frequently happens in most surfaces [54, 57]. As shown in Fig. 7, the NF90 membrane has an outstanding high roughness.

After being used to filter KCA, the tendency is similar for the NF, NP030, and NP010, but this behavior does not occur in the case of the NF90 membrane which in principle should have this plateau for higher values of L. This may be due to its high initial roughness. The three membranes with low roughness have different changes in their original roughness. While NP030 and the NF increase their roughness, the NP010 one decreases as a result of the KCA adsorption. However, the three membranes tend to a similar roughness value which should correspond to a compact surface of KCA. In these conditions, their roughness is between 15 and 20 nm after KCA use (amplified inset in Fig. 8b).

The results reported on the roughness of fouled membranes are complicated to compare to each other due to the complex nature of foulants and particular interactions with each membrane type and composition that leads to a diversity of interpretations of the changes detected [57].

It seems clear that the NF90 membrane has a small adsorption of KCA, which can be confirmed by the small change in its high roughness and by the slight reduction of its permeability. According to Yangali-Quintanilla et al. [58], the NF90 membrane presents a quite different behavior because they observed a reduction in the surface roughness which should be attributed to a higher adsorption of the fouling agent, sodium alginate, used by these authors. The value found for the NF90 roughness is very similar to that found by Xu et al. [59]. In their study, they found the value of surface roughness for the NF90 to be 63.9 nm. On the other hand, the value found by Nghiem et al. [15], 76.8 nm, is quite different. For the NP010 membrane, the roughness found is very different from that found by Boussu et al. [36], which was of 2.4 nm for a 3×3 mm scanned area. On the other hand, the NP030 membrane presents a similar roughness to that also found in Boussu et al. [36], which was of 3.4 nm, also for the same scanned area. Nevertheless, these values refer to membranes treated at pH 6.

It seems clear that rough surfaces present more adsorption surface area than smooth surfaces [11, 13, 25, 34] made from the same material especially when fouling is high as for the polyethersulfone membranes (NP030 and NP010). Therefore, in this case particles are accumulated preferentially in the "valleys" than in the peaks, resulting in "valley clogging" that for membranes showing low affinity for the KAC (NF90 and NF) is avoided due to the sweeping effect of the retentate agitation. In Fig. 9, we suggest a scheme that could explain how the roughness is modified after KCA filtration by taking into account the corresponding changes in permeability too. The gray lines represent the profile of a cross section of the membrane surface, and the black balls represent the molecules or molecular aggregates of KCA. The polyamide membranes, NF90 and NF, have a lower reduction in permeability after contacting KCA and the roughness of the used membranes increases slightly as compared with those of the clean membrane. This behavior is consistent with the scheme of Fig. 9, where only a small amount of molecules are adsorbed on the surface. In contrast, the polyethersulfone membranes, NP030 and NP010, have a high reduction of permeability while their roughness tends to a similar value. This suggests that there is a high affinity between the polyethersulfone surface and the KCA molecules or

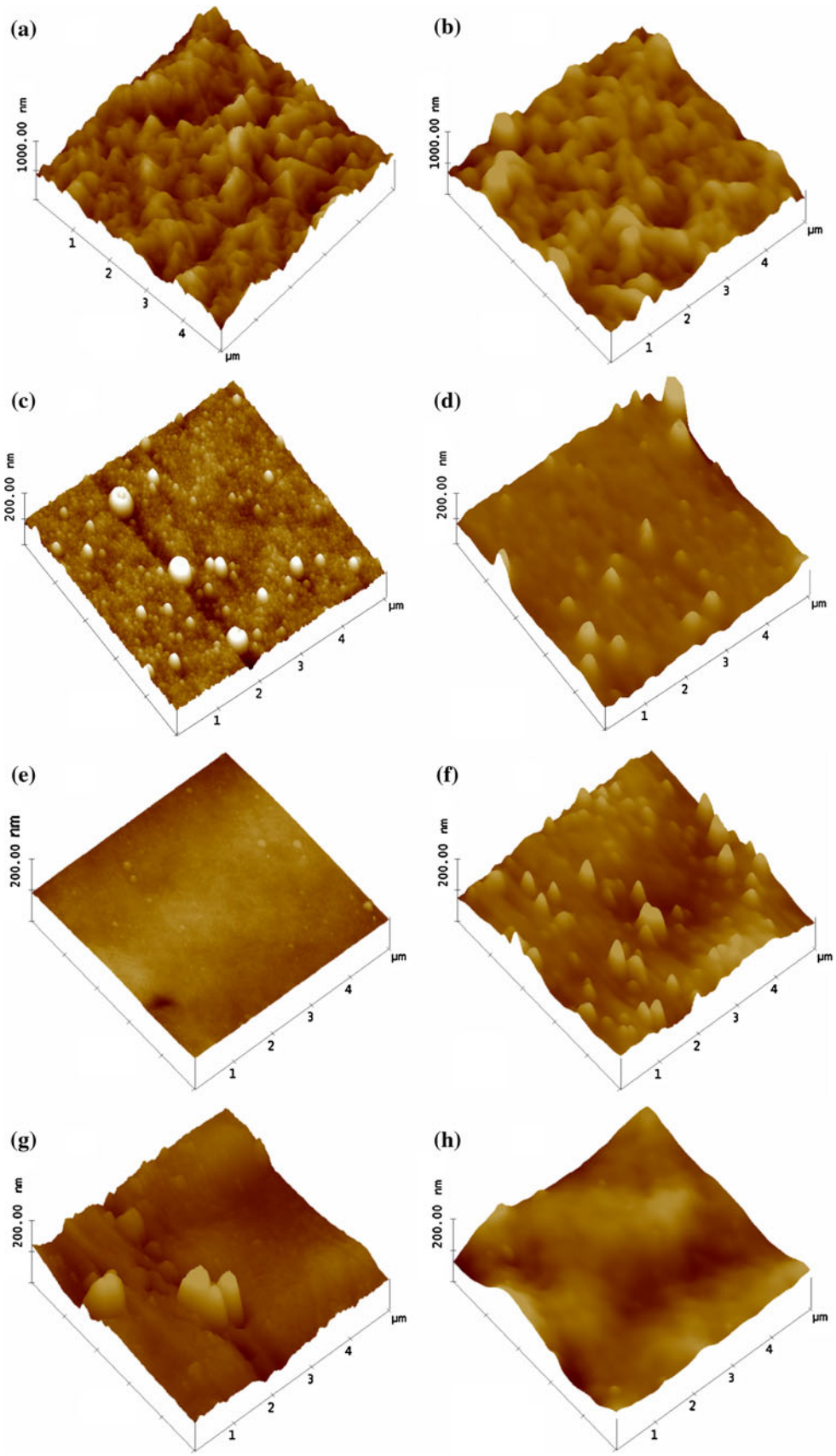

Fig. 7 3D-AFM images corresponding to scanned areas of 5 × 5 µm^2 for: **a** NF90 clean and **b** used, **c** NF clean and **d** used, **e** NP030 clean and **f** used, and **g** NP010 clean and **h** used

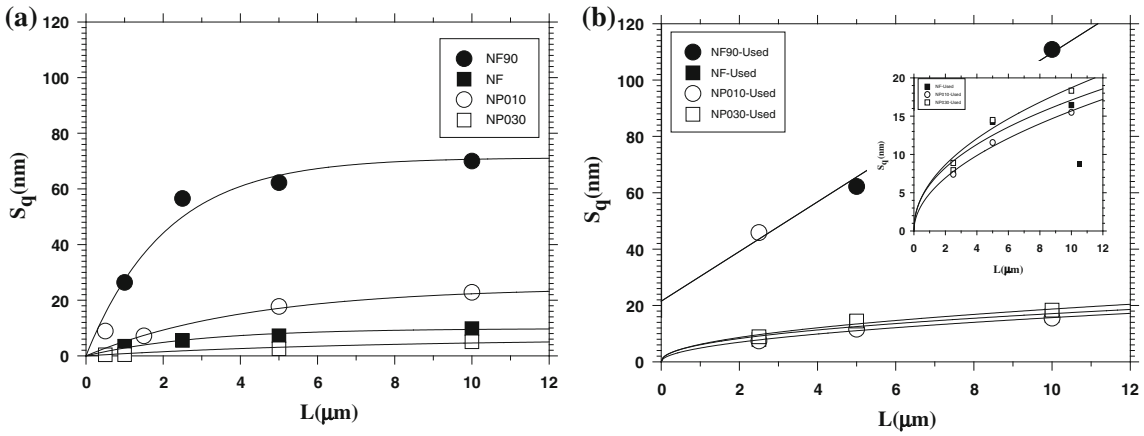

Fig. 8 Roughness, S_q, as a function of the length scale, L, (side of the square scanned area) for all the membranes studied before (**a**) and after (**b**) fouling with KCA. The inset shows a detail of the three membranes with low and very similar roughness (NF90, NP030, and NP010)

aggregates and the high flows produce a multilayer of KCA which gives a roughness value mainly due to clavulanate which masks the initial topography of the membrane surface.

The analysis of the roughness of these membranes shows that the NF90 membrane has a far greater roughness than the others, up to almost an order of magnitude. A high roughness in a nanofiltration membrane may be intentional to reduce the fouling process by creating micro or nano-turbulences on the membrane surface, thus increasing the coefficient of mass transfer [60]. For this reason when trying to correlate surface parameters of these membranes with flow and structural parameters, the NF90 membrane is out of the trend. As mentioned in the introduction, Hirose et al. [61] have found a linear relationship with positive slope between the roughness and the permeability for several reverse osmosis membranes made from the same crosslinked aromatic polyamide. These authors attributed the linear relationship they found the surface unevenness of the membranes, which should resulted in an enlargement of the effective membrane area. In our case NF, NP030, and NP010 membranes follow this tendency before their use with KCA as shown in Fig. 10, for images of 2.5 × 2.5 μm in size. The NF90 membrane is placed far away from the trend with the highest value of roughness and the lowest permeability. As expected the membranes used with KCA loose totally this correlation.

All correlations of roughness with other functional parameters suffer the lack of definition of roughness that, as clearly shown in Fig. 8, changes with the scanned area. One way to avoid this problem is to use the Power Spectra Density (PSD) of the surface according to Eq. 6 as discussed above in section 2.4. Figure 11 shows an example of the spectrum for the clean NF membrane for three different scan sizes. One can see that in the central part of the spectrum, the slope is very similar for all scan sizes. This

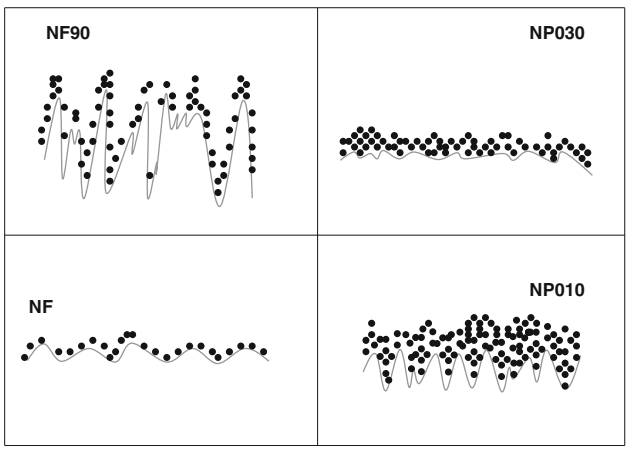

Fig. 9 Scheme of the cross section for the deposition of KCA (*black balls*) according to the fouling mechanism assumed on the surface (*gray line*) of each membrane studied

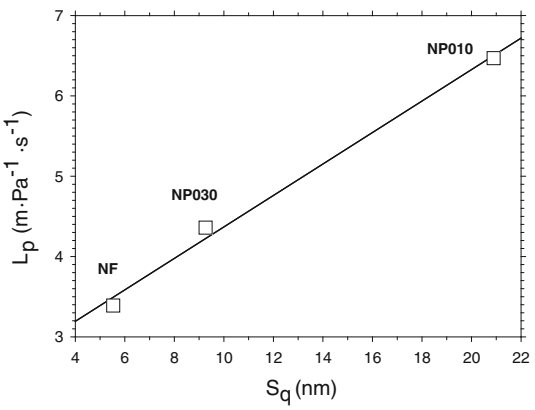

Fig. 10 Experimental water permeability versus roughness, S_q, as obtained from images with scanned areas of 2.5 × 2.5 μm of the clean membranes

makes this technique clearly more powerful than the simple analysis of the roughness at given scanned areas. As mentioned, the slope of the spectrum allows evaluating the fractal dimension according to Eq. 10. When the slope decreases the fractal dimension increases, which corresponds to a surface that fills more the space, thus looking denser [24]. Table 4 shows the fractal dimension of the membranes studied before and after filtration of the KCA.

It is noted that in this case there is always an increase in fractal dimension of the membrane (denser surface) due to the fouling process. This increase appears also for the NP010 membrane that shows a decrease in its surface roughness after being used (see Fig. 8b). This difference in trend may be due to the highest error implicit in the method of analysis of the simple roughness. On the other hand, the fractal dimension is also connected with the lateral distribution of height deviations so is a more robust way to characterize the rough or flat nature of the surface. As a result, it can be concluded that the vertical profile of the surface of the NP010 membrane is flattened after interaction with KCA but the new surface fills more the space horizontally.

If the variation in fractal dimension, D, is related to the adsorption of KCA which is correlated with variations in permeability, these two magnitudes should be correlated as well. Figure 12 shows the percentage of the initial (new membrane) permeability that remains after KCA filtration versus the difference in fractal dimension between the fouled membrane, D_f and the clean (unused one), D_i. It is noted that the membranes which have similar values of roughness before KCA use (NF, NP030, and NP010) can be fitted to an exponential decay. The NF90 membrane is clearly out of this relationship because, as mentioned above, it has a roughness three times greater than the other membranes.

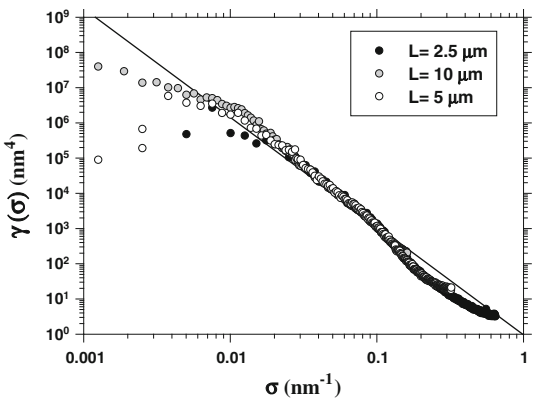

Fig. 11 2D Power Spectra Density of NF clean membrane with several scan sizes. The fitted line (which slope determines the fractal dimension) corresponds to the best fitting to the three length scales (side of the square scanned area) shown

Table 4 Fractal dimension for the clean and fouled membranes

Fractal dimension	NF90	NF	NP030	NP010
Clean	2.10 ± 0.02	2.14 ± 0.03	2.40 ± 0.04	2.50 ± 0.04
Fouled	2.45 ± 0.08	2.26 ± 0.05	2.72 ± 0.07	2.63 ± 0.05

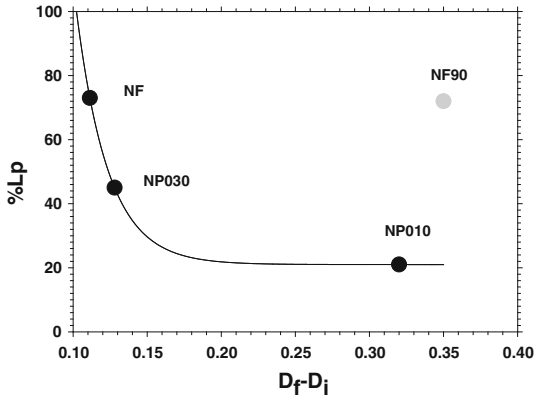

Fig. 12 Percent reduction of the permeability due to the KCA adsorption versus the difference of the fractal dimension of the clean membrane, D_i and the used one D_f

Finally, we have calculated the skewness of the heights distribution on the surface of the membranes using Eq. 11. The values are positive in all cases which indicate that these surfaces have high spikes that protrude over a flatter average [54]. Comparing the results of the membranes before and after filtration with KCA is observed that for the polyamide membranes, NF and NF90, the value of the skewness increases, whereas those of polyethersulfone this trend is not so clear. Possibly in this case the highly coating layer of KCA molecules (on an initial relatively flat surface) does not follow a trend. The kurtosis has been computed using Eq. 12. For all membranes, except for NP010, it is observed an increase in kurtosis, indicating that the protuberances on the surface have more similar sizes after adsorption of the KCA. In contrast, for the NP010 it is observed a decreasing kurtosis, indicating a wider distribution of the heights of the surface. This must be the result of high accumulation of aggregates of KCA, such as all data have indicated.

Conclusions

The AFM technique allows a determination of the pore size distribution of membranes with pore sizes in the order of the nanometer when the surface roughness of the samples is low.

The results have been correlated with the permeability of the clean membrane and indicate that at least a proportion of the pores have slit-type geometry.

The analysis of height difference in the surface images before and after the filtering process of KCA has been studied by using: Root Mean Square roughness, S_q, Power Spectra Density, PSD, Fractal dimension, D, Skewness, S_{sk}, and Kurtosis, S_{ku}.

These parameters have been related to the permeability, the type of material, the amount of adsorbed solute on the surface and the pore size.

It is noted that for membranes with similar (here low) values of the initial roughness:

- The initial experimental permeability is linearly related to that evaluated from the pore size distributions.
- If the adsorption layers of KCA are enough, the roughness tends to a similar value for all membranes.
- The fractal dimension increases in every case after the adsorption process, which is in agreement with the densification of the surface.
- The permeability reduction is higher the greater is the difference between the fractal dimension before and after the adsorption.

Acknowledgements Brazilians authors acknowledge the financial support from the Coordenação de Aperfeiçoamento de Pessoal de Nível Superior (CAPES) and the State of São Paulo Research Foundation (FAPESP). Spanish authors want to thank the "Ministerio de Ciencia e Innovación (MCINN)" for financing this study within the frame of the "Plan Nacional de I+D+I" and through the project CTQ2009-07666. Also the Spanish "Junta de Castilla y León" has contributed through the project Grupos de Excelencia-GR18. The authors also acknowledge Filmtec™ and Microdyn Nadir® fir the donation of the membranes.

References

1. Hilal N, Al-Zoubi H, Darwish NA, Mohammad AW, Abu Arabi M (2004) Desalination 170:281
2. Bowen WR, Mohammad AW, Hilal N (1997) J Membr Sci 126: 91
3. Mohammad AW, Hilal N, Seman MNA (2005) J Appl Polym Sci 96:605
4. Bargeman G, Vollenbroek JM, Straatsma J, Schroën CGPH, Boom RM (2005) J Membr Sci 247:11
5. Bowen WR, Doneva TA (2000) J Colloid Interface Sci 229:544
6. Otero JA, Mazarrasa O, Villasante J, Silva V, Prádanos P, Calvo JI, Hernández A (2008) J Membr Sci 309:17
7. Singh S, Khulbe KC, Matsuura T, Ramamurthy P (1998) J Membr Sci 142:111
8. Prádanos P, Rodriguez ML, Calvo JI, Hernández A, Tejerina F, de Saja JA (1996) J Membr Sci 117:291
9. Ochoa NA, Prádanos P, Palacio L, Pagliero C, Marchese J, Hernández A (2001) J Membr Sci 187:227
10. Koyuncu I, Brant J, Lüttge A, Wiesner MR (2006) J Membr Sci 278:410
11. Wong PCY, Kwon Y-N, Criddle CS (2009) J Membr Sci 340:117
12. Schäfer AI, Fane AG, Waite TD (2000) Desalination 131:215
13. Vrijenhoek EM, Hong S, Elimelech M (2001) J Membr Sci 188:115
14. Koros WJ, Ma YH, Shimidzu T (1996) J Membr Sci 120:149
15. Nghiem LD, Vogel D, Khan S (2008) Water Res 42:4049
16. Bhattacharyya D, Hestekin J, Shan D, Ritchie S (2002) J Chin Inst Chem Eng 33:61
17. Van der Bruggen B, Vandecasteele C, Van Gestel T, Doyen W, Leysen R (2003) Environ Prog 22:46
18. Koyuncu I, Turan M, Topacik D, Ates A (2000) Water Sci Technol 41:213
19. Van der Bruggen B, Kim JH, DiGiano FA, Geens J, Vandecasteele C (2004) Sep Purif Technol 36:203
20. Vrouwenvelder JS, Kappelhof JWNM, Heijman SGJ, Schippers JC, Van der Kooij D (2003) Desalination 157:361
21. Tarabara VV, Koyuncu I, Wiesner MR (2004) J Membr Sci 241:65
22. Van der Bruggen B, Vandecasteele C (2001) Environ Sci Technol 35:3535
23. Van der Bruggen B, Braeken L, Vandecasteele C (2002) Desalination 147:281
24. Wyart Y, Georges G, Deumié C, Amra C, Moulin P (2008) J Membr Sci 315:82
25. Elimelech M, Zhu X, Childress AE, Hong S (1997) J Membr Sci 127:101
26. Sheldon JM (1991) J Membr Sci 62:75
27. Bessières A, Meireles M, Coratger R, Beauvillain J, Sanchez V (1996) J Membr Sci 109:271
28. Wei Q, Wang D (2003) Mater Lett 57:2015
29. Bowen WR, Hilal N, Lovitt RW, Willians PM (1996) J Membr Sci 110:229
30. Bowen WR, Hilal N, Lovitt RW, Willians PM (1996) J Membr Sci 110:233
31. Hilal N, Bowen WR (2002) Desalination 150:289
32. Hilal N, Al-Zoubi H, Darwish NA, Mohammad AW (2005) Desalination 177:187
33. Boussu K, Van der Bruggen B, Volodin A, Snauwaert J, Van Haesendock C, Vancasteele C (2005) J Colloid Interface Sci 286:632
34. Boussu K, Van der Bruggen B, Volodin A, Van Haesendonck C, Delcour JA, Van der Meeren P, Vandecasteele C (2006) Desalination 191:245
35. Lu Y, Suzuki T, Zhang W, Moore JS, Mariñas BJ (2007) Chem Mater 12:3194
36. Boussu K, Vandecasteele C, Van der Bruggen B (2008) J Membr Sci 310:51
37. El-Said WH, Yea C-H, Jung M, Kim H, Choi J-W (2010) Ultramicroscopy 110:676
38. Jaafar M, Navas D, Hernández-Vélez M, Balñdonedo JL, Vázquez M, Asenjo A (2009) Surf Sci 603:3155
39. Popa AM, Angeloni S, Bürgi T, Hubbell JA, Heinzelmann H, Pugin R (2010) Langmuir 26:15356
40. De-Lima LC, De-Macedo MMG, De-Alburquerque M, De-Alburquerque M, Simão RA (2009) Nano 4:157
41. Howarth TT, Brown AG, King TJ (1976) J Chem Soc, Chem Commun 7:266
42. Vandamme EJ (1984) Clavulanic acid: properties, biosynthesis and fermentation (biotechnology of industrial antibiotics 22). Marcel Dekker, New York
43. Bersanetti PA, Almeida RMRG, Barboza M, Araújo MLGC, Hokka CO (2005) Biochem Eng J 23:31
44. Almeida RMRG, Barboza M, Hokka CO (2003) Appl Biochem Biotechnol 108:867
45. Bowen WR, Welfoot JS (2002) Desalination 147:197
46. Calvimontes A, Stamm M, Dutschk V (2009) Tenside Surfact Det 46:368

47. Nghiem LD, Shafer AI, Elimelech M (2005) Sep Sci Technol 40:2633
48. López-Muñoz MJ, Sotto A, Arsuaga JM, Van der Bruggen B (2009) Sep Purif Technol 66:194
49. Giessibl FJ (2003) Rev Mod Phys 75:949
50. Walsh CJ, Leistner AJ, Oreb BF (1999) Appl Opt 38:4790
51. Church EL (1988) Appl Opt 27:1518
52. Deumié C, Richier R, Dumas P, Amra C (1996) Appl Opt 35:5583
53. Ruppe C, Duparré A (1996) Thin Solid Films 288:8
54. Mendez-Vilas A, Bruque JM, González-Martín ML (2007) Ultramicroscopy 1007:617
55. Wesolowska K, Koter S, Bodzek M (2004) Desalination 162:137
56. Montalvillo M, Silva V, Palacio L, Calvo JI, Hernández A, Pradanos P (2011) J Phys Chem (submitted)
57. Macanás J, Palacio L, Prádanos P, Hernández A, Muñoz M (2006) Appl Phys A Mater Sci Process 84:277
58. Yagali-Quintanilla V, Sadmani A, McConville M, Kennedy M, Amy G (2009) Water Res 43:2349
59. Xu P, Drewes JE, Kim T-U, Bellona C, Amy G (2006) J Membr Sci 279:165
60. Izák P, Godinho MH, Brogueira P, Figueirinhas JL, Crespo JG (2008) J Membr Sci 321:337
61. Hirose M, Ito H, Kamiyama Y (1996) J Membr Sci 121:209